Journal of Structural Geology 31 (2009) 1062–1073

Contents lists available at ScienceDirect

Journal of Structural Geology

journal homepage: www.elsevier.com/locate/jsg

Quantitative correlation of texture and magnetic anisotropy of compacted calcite–muscovite aggregates

Volkmar Schmidt [a,1], Ann M. Hirt [a,*], Bernd Leiss [b], Luigi Burlini [c], Jens M. Walter [d]

[a] Institute for Geophysics, ETH Zurich, Sonneggstrasse 5, CH-8092 Zurich, Switzerland
[b] Institute for Geology, ETH Zurich, CH-8092 Zurich, Switzerland
[c] GZG, University of Göttingen, D-37077 Göttingen, Germany
[d] Forschungszentrum Jülich, D-52425 Jülich, Germany

ARTICLE INFO

Article history:
Received 27 June 2008
Received in revised form
3 November 2008
Accepted 26 November 2008
Available online 7 December 2008

Keywords:
Compaction
Magnetic anisotropy
Calcite
Muscovite
Neutron diffraction
Texture

ABSTRACT

Deformation of carbonate rocks leads to crystallographic preferred orientations (CPOs) of calcite, which in turn generates an anisotropy of magnetic susceptibility (AMS). The use of the diamagnetic anisotropy, which arises from the preferential orientation of calcite, for texture characterization is usually hindered by (1) the weakness of the anisotropy, and (2) overlapping contributions from paramagnetic and ferromagnetic minerals to the AMS. In this study, the diamagnetic, paramagnetic and ferromagnetic sub-fabrics of synthetic calcite–muscovite samples have been separated using high-field torque measurements. The CPO of calcite and muscovite has been determined by neutron diffraction, and the magnetic sub-fabrics are compared to the AMS that was re-calculated from the CPO. The isolated diamagnetic sub-fabric shows a good correlation with the calcite texture for calcite concentrations above 70%. The paramagnetic sub-fabric is shown to be a reliable texture parameter for muscovite, even at a concentration of 5%. The results demonstrate the capability of the AMS method as a texture parameter in impure carbonate rocks.

1. Introduction

The anisotropy of magnetic susceptibility (AMS) is a physical property of rocks, and arises from (i) the minerals, which contribute to the AMS signal; (ii) the single crystal anisotropy of constituent minerals; and (iii) the degree of preferential orientation of minerals, i.e., texture. For this reason, it is often named the magnetic fabric of a rock. Since preferred orientations can be induced by deformation, the AMS can serve as a strain indicator in various rock types (cf., Hrouda, 1982; Borradaile and Henry, 1997; Borradaile, 1988). Important in this case is that there is a good understanding of the three controlling factors outlined above. This is not always straightforward when dealing with natural rocks.

The correlation of AMS with deformation was first applied to rocks whose AMS was carried by accessory iron oxides (Graham, 1954; Uyeda et al., 1963). The importance of paramagnetic minerals as carriers of the magnetic fabric became more apparent with further investigations (e.g., Coward and Whalley, 1979; Rochette and Vialon, 1984). The comparison of AMS with X-ray and neutron diffraction (e.g., Kligfield et al., 1983; Hirt et al., 1995; Siegesmund et al., 1995; Lüneburg et al., 1999; Chadima et al., 2004) showed that the AMS of phyllosilicate-bearing rocks reflects their crystallographic preferred orientation (CPO, texture). Therefore several researchers have suggested that only the paramagnetic AMS be used in a quantitative correlation between AMS of a rock and mineral fabric (e.g., Hrouda et al., 1997; Hirt et al., 2004; Cifelli et al., 2005).

In carbonate rocks, the CPO of calcite is indicative of deformation history (e.g., Wenk et al., 1987; Ratschbacher et al., 1991; Lafrance et al., 1994; Rutter et al., 1994; Bestmann et al., 2000; Leiss and Molli, 2003; Trullenque et al., 2006) and it generates an AMS due to the relatively strong diamagnetic anisotropy of calcite. Therefore, a quantitative correlation between AMS and strain was established for an experimentally deformed Carrara marble (Owens and Bamford, 1976; Owens and Rutter, 1978), in spite of low bulk susceptibility. However, only a single tectonic field study used the AMS due to calcite alone as a deformation marker (de Wall et al., 2000). This reflects the difficulties in measuring a weak diamagnetic anisotropy that is usually overprinted by contributions from ferromagnetic or paramagnetic minerals (e.g., Lowrie and Hirt, 1987; Jackson, 1990; Lagroix and Borradaile, 2000; Evans et al., 2003; Piper et al., 2007). A further complication arises when ferrous iron substitutes for calcium in the carbonate structure, so that an

* Corresponding author. Tel.: +41 44 633 2705; fax: +41 44 633 1065.
E-mail address: ann.hirt@erdw.ethz.ch (A.M. Hirt).
[1] Present address: K-UTEC AG Salt Technologies, D-99706 Sondershausen, Germany.

0191-8141/$ – see front matter © 2008 Published by Elsevier Ltd.
doi:10.1016/j.jsg.2008.11.012

Fe^{2+} content >400 ppm leads to inverse magnetic fabric, i.e., the maximum and minimum axes of the susceptibility ellipsoid are switched (Rochette, 1988; Ihmlé et al., 1989; Schmidt et al., 2007a). In this case the maximum axes of the susceptibility ellipsoid will be sub-parallel to the pole of tectonic flattening.

Methods for the separation of the ferromagnetic and paramagnetic sub-fabrics of rocks were developed using high-field torque methods at room temperature (Martín-Hernández and Hirt, 2001, 2004; Martin-Hernandez and Ferré, 2007). Recently, a new method was developed for the isolation of diamagnetic sub-fabrics using low-temperature measurements (Schmidt et al., 2007b). This method has enabled us to investigate the AMS due to calcite in impure carbonate rocks. Therefore, the AMS in calcite-rich rocks with respect to deformation textures can be investigated in the context of the three sources for the AMS: paramagnetism, ferromagnetism and diamagnetism.

In this study, we investigate the relationships between deformation, CPO and AMS on synthetic muscovite–calcite aggregates, so that we have control on the exact composition and degree of deformation that the samples have undergone (Schmidt et al., 2008). By eliminating unknowns encountered when dealing with natural rocks, we can better understand the factors that influence the AMS in natural carbonate rocks. The samples were fabricated from powders by experimental compaction and annealing. The volume-related CPO of calcite and muscovite was determined by neutron diffraction on the same samples used for the AMS measurements; therefore the same volume of material was considered in both measurements. The diamagnetic, ferromagnetic and paramagnetic sub-fabrics were separated by high-field torque measurements and compared to the values modeled from the CPO. In the following sections, the term *texture* refers to the CPO, whereby the AMS is called the magnetic fabric. The AMS due to an individual mineral fraction is called a magnetic sub-fabric.

2. Methods and samples

2.1. Sample preparation and description

The synthetic samples were fabricated from calcite and muscovite powders with known magnetic properties. The preparation, microstructure and the physical properties of the samples are described in Schmidt et al. (2008). The calcite powder was ground from pure Carrara marble, and the muscovite powder from commercially available pegmatitic muscovite crystals. Because of the large amount of muscovite needed, the muscovite crystals had to be purchased in three batches. The crystals from these batches had different magnetic properties, which we refer to as "Mu1", "Mu2", and "Mu3". The susceptibility of the calcite powder was -12.0×10^{-6} SI and that of the muscovite powder between 88×10^{-6} SI and 105×10^{-6} SI. The muscovites had a similar chemical composition and contained 1.0–1.2 wt% iron. The powders were mixed in different proportions and uniaxially cold-pressed in stainless steel cylinders under varying loads up to 400 MPa to produce a CPO (texture). Annealing by hot isostatic pressing (HIPping) generated firm samples. A core with diameter of 2.54 cm was drilled out of the cylinder and was cut into several specimens. Specimens with a length of 2.2 cm were used for magnetic and neutron diffraction measurements (Table 1). The homogeneity of the texture throughout the sample has been proven by X-ray diffraction measurements on several slices of a sample (Schmidt et al., 2008). The calcite fraction shows a wide grain-size distribution ranging from <0.5 μm to 80 μm. The different grain-size fractions are homogeneously distributed. Calcite grains are frequently strongly twinned, and show no significant shape-preferred orientation. The muscovite fraction also shows a wide grain-size distribution with maximum grain sizes of 100 μm. The grains have their basal planes oriented normal to the compression direction and are often bent and kinked.

2.2. Texture analysis

The analysis of the calcite and muscovite textures was based on neutron diffraction measurements conducted with the SV7-b texture diffractometer at the FRJ-2 research reactor of the Forschungszentrum Jülich, Germany. The texture diffractometer SV7-b works with a monochromatic beam of a constant wavelength of 2.332 Å and a resolution of $\Delta d/d = 1.3 \times 10^{-2}$ (Jansen et al., 2000). The detector allows the measurement of a diffraction pattern in a maximum range of $2\theta = 60^{\circ}$, which is equivalent to a d-range of 6.11–1.77 Å. Peak intensities of the diffraction patterns are interpolated in pole figures with an equal-area grid of $5^{\circ} \times 5^{\circ}$ and a projection in the lower hemisphere. All pole figures presented here are experimental pole figures with maxima given as multiples of random distribution (m.r.d.).

The calcite basal planes (0 0 1), which correspond to the c-axes, are represented by the (0 0 6) peak in the diffraction pattern (Fig. 1). The basal planes of the muscovite are represented by three peaks: the (0 0 4), (0 0 6) and the (0 0 10) peak. Pole figures from all three muscovite peaks show the same type of orientation distribution. The intensities, however, differ considerably. To analyze the experimental diffraction patterns a diffraction pattern of the muscovite powder was measured. Since the structure parameters of muscovite can vary extensively, measuring the actual muscovite powder is more reliable than using calculated standard or other reference patterns. As the (0 0 4) muscovite peak has a very low intensity and is situated at the margin of the diffraction spectrum (Fig. 1), its statistical error is the highest of the three basal plane reflections. The (0 0 6) muscovite peak overlaps with the (0 2 4) peak of muscovite with an intensity ratio of about 5:2. These two muscovite peaks cannot be separated, as the spectral resolution is too low. From the comparison of this (006)/(024)-pole figure with the (004)-pole figure it is obvious, that the pole figure type does not change.

Table 1
Overview of specimens used in this study.

	Hand pressed	20 MPa	40 MPa	100 MPa	200 MPa	400 MPa
0% mu	0-5-0	0-20-4	0-40-0	0-100-1	0-200-0	0-400-1
5% mu1	5-5-0	5-20-0	5-40-2	5-100-4	5-200-2	5-400-2
10% mu1	–	10-20-3	–	10-100-2	10-200-3	–
30% mu2	–	30-20-2	–	30-100-2	30-200-2	–
50% mu2	–	50-20A-2	–	50-100A-2	50-200A-2	–
50% mu3	–	50-20B-S	–	50-100B-S	50-200B-S70-200-0	–
70% mu3	–	70-20-0 –	–	70-100-070-100-R		
100% mu3	–	100-20-0	–	100-100-0	100-200-0	–

mu: Muscovite concentration in the samples.

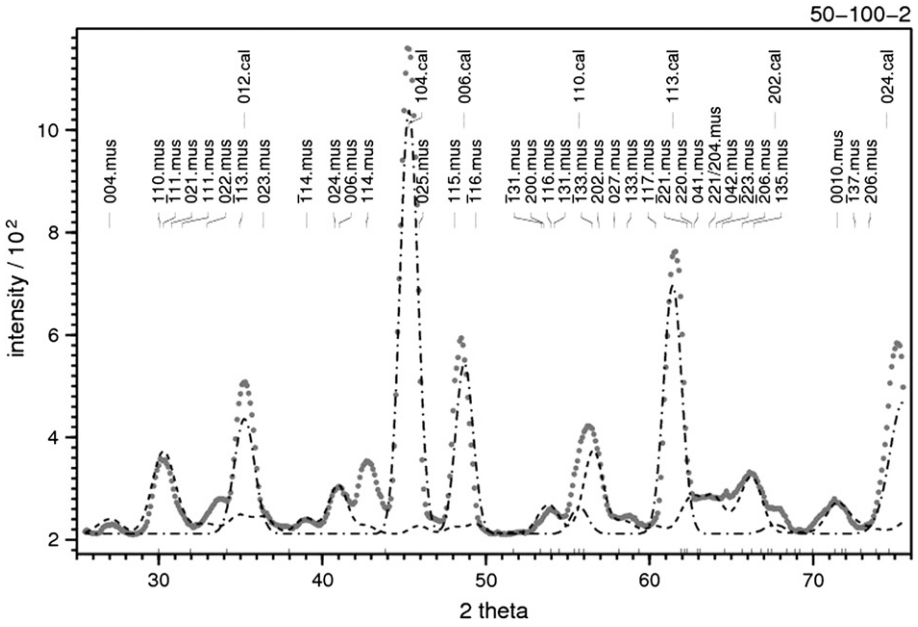

Fig. 1. Mean neutron diffraction spectrum of sample 50-100-2 consisting of 50% calcite and 50% muscovite. The dotted grey line represents the measured diffraction pattern. The dashed line is the muscovite powder diffraction spectrum and the dotted-dashed line is a theoretical spectrum of calcite (ICSD 18165).

However, the intensity of the (006)/(024)-pole figure is lower, since the additional (024)-reflections randomize a certain portion of the bulk intensity. The (0 0 10) peak of muscovite is also overlapped by other reflections of muscovite (not all are listed in Fig. 1), but they have very low intensity and therefore are neglected for this study. Based on these observations, the (0 0 10) pole figure is regarded as the most reliable pole figure to represent the CPO of muscovite.

The *c*-axis orientation tensors **t** for calcite and muscovite were calculated from the respective pole density distributions (Woodcock, 1977; Cheeney, 1983). The eigenvalues and eigenvectors of **t** define the texture ellipsoid. Its eigenvalues t_i, $i=1, 2, 3$, were normalized to one, i.e., $t_1+t_2+t_3=1$. A perfect alignment of the *c*-axes results in $t_1=1$ and $t_2=t_3=0$, whereas $t_1=t_2=t_3=1/3$ describes a perfectly random distribution. The parameter $\Delta t=t_1-t_3$ is used to describe the intensity of the texture, which is justified for nearly uniaxial CPOs. N.B., the AMS due to an arbitrary *c*-axis distribution with the texture tensor **t** is the same as that of a *c*-axis distribution composed of three volume fractions equal to $t_i, i=1,2,3$, which are aligned in the respective directions of the eigenvector of t_i.

2.3. AMS and separation of sub-fabrics

The magnetic susceptibility is described by a symmetric second-rank tensor **k** with the eigenvalues k_1, k_2, and k_3 ($k_1 \geq k_2 \geq k_3$), where $k_M=(k_1+k_2+k_3)/3$ is the mean susceptibility. The tensor is geometrically represented by an ellipsoid, in which k_1, k_2 and k_3 are the lengths of the principal axes. The anisotropic part of **k** is called the deviatoric susceptibility tensor **l** (Jelinek, 1985); it is

$$\mathbf{l} = \mathbf{k} - k_M\mathbf{E}$$

where **E** is the unit matrix, and

$$l_{11}+l_{22}+l_{33} = 0.$$

The susceptibility ellipsoid is described below with the parameters Δk and U, which can also be calculated from the deviatoric tensor, which is measured with a torque magnetometer. The difference between maximum and minimum susceptibility is $\Delta k=k_1-k_3$. For uniaxial AMS shapes, Δk is a direct measure of the intensity of the anisotropy. U is a shape parameter where $U=(2k_2-k_1-k_3)/(k_1-k_3)$ (Jelinek, 1981); $U=1$ for perfectly oblate shapes, $U=-1$ for perfectly prolate shape, and $U=0$ when $k_1-k_2=k_2-k_3$.

Low-field AMS (LF-AMS) was measured at room temperature with a KLY-2 and a KLY-4 susceptibility meter (AGICO, Brno), respectively, in an alternating field of 300 A/m. The mean susceptibility was calculated from the full susceptibility tensor. *F*-tests for determining the plane of flattening of the AMS ellipsoids were significant at the 95% confidence level for all samples. High-field AMS (HF-AMS) was measured with the torque magnetometer at the Laboratory for Natural Magnetism at the ETH Zurich (Bergmüller et al., 1994). This device measures susceptibility differences in a plane and only the deviatoric part of the susceptibility tensor is obtained. Using a fast measurement mode, the sensitivity of the instrument is about 3×10^{-8} (SI) for a sample size of 10 cm^3 (Schmidt et al., 2007b) and the AMS was reproducible within this limit. The HF-AMS was measured at room temperature and at 77 K using at least four fields between 600 mT and 1500 mT. Because of the weak anisotropy of the samples measuring the background signal of the holder and subtracting it from the torque curves was important.

The ferrimagnetic, paramagnetic and diamagnetic anisotropies were separated using the methods described in Martín-Hernández and Hirt (2001) and Schmidt et al. (2007a). The contribution of hematite to the AMS was determined for one sample by measurement in six fields (Martín-Hernández and Hirt, 2004). For the separation of paramagnetic and diamagnetic AMS, the increase in Δk upon cooling to 77 K (p_{77}-factor, Schmidt et al., 2007a,b) of the paramagnetic minerals must be known. The value was determined by measuring the torque of pure muscovite samples at room temperature and at 77 K. Note, that muscovite is regarded as the paramagnetic fraction, although it also possesses a diamagnetic anisotropy. Measurements of flakes of Mu3 before axial compaction and the pure muscovite samples 100-100 gave slightly different p_{77}-values of 8.7 and 8.23, respectively. The difference could be due to compositional changes during HIPping, for instance formation of magnetite/maghemite from iron in muscovite or changes in the diamagnetic anisotropy of muscovite by dehydroxylation (Gehring et al., 1993). Therefore, determination of the *p*-value from untreated samples of Mu1 and Mu2 was rejected and $p_{77}=8.23$ was used for

the separation of all samples. This assumption is sound, since all three batches of muscovite had similar iron content, and p did not change significantly with axial load; p_{77} was 8.23 for samples 100-20 and 100-100 and 8.34 for 100-200. Therefore, the uncertainty in the p-value is below 0.5 for the individual specimen. Furthermore, the method for isolating the diamagnetic sub-fabric assumes perfectly uniaxial AMS of the paramagnetic minerals. However, single crystals of muscovite have been shown to possess a triaxial-oblate AMS with U ranging from 0.6 to 0.8 (Borradaile and Werner, 1994; Martín-Hernández and Hirt, 2003). We assume that the triaxial shape arises from anisotropy in the basal plane. Fe^{2+} ions in the dioctahedral muscovite are located in the *cis*-coordinated octahedrons (Ballet and Coey, 1982; Bailey, 1984), which are not randomly distributed in a 2:1 layer. This leads to anisotropy in the Fe^{2+} distribution and magnetic susceptibility in such a layer. Stacking of the layers in the 3T or 6H polytypes can randomize the anisotropy; however, these polytypes are very rare amongst natural muscovite crystals (Bailey, 1984). Since the a-axes of the samples in this study have no preferred orientation in the compressional plane, a possible magnetic anisotropy in the basal planes of the single crystal cancels out in the polycrystals and the use of the separation method is justified.

2.4. Isothermal remanent magnetization (IRM) acquisition

The acquisition of IRM was used to identify ferromagnetic phases in the samples. The samples were magnetized with a pulse magnetizer (ASC Scientific, IM-10-30) first in one direction along the sample cylinder axis in a field of 2.5 T, and then in the opposite direction in progressively higher fields from 10 mT up to 2.5 T. This procedure allows the coercivity of remanence H_{cr} and the saturation remanent magnetization M_{rs} to be determined. For samples that were not saturated in the highest applied field, the value of M_{rs} is the remanent magnetization at 2.5 T. H_{cr} is indicative of the ferromagnetic minerals in the sample, e.g., magnetite has H_{cr} from 10 to 50 mT and hematite shows values of some hundred milliteslas. M_{rs} is indicative of the concentration of the ferromagnetic phase in the sample.

2.5. Calculation of the theoretical AMS

The AMS of a polycrystalline aggregate results from the CPO of the minerals and their intrinsic AMS. For the calculation of the AMS due to minerals with a uniaxial intrinsic AMS, the directional distribution of the pole to the isotropic plane is sufficient (Owens, 1974). In the case of calcite and muscovite, these poles are the orientation distributions of the c-axes. The diamagnetic and paramagnetic deviatoric susceptibility tensors were modeled from the c-axis CPOs of calcite and muscovite, respectively, using the method described in Martín-Hernández et al. (2005). The deviatoric susceptibility tensor $\mathbf{I}^{\text{model}}$ is obtained by integration of the probability density $P(\theta,\varphi)$ multiplied by the deviatoric susceptibility tensor $\mathbf{I}$ of the single crystal rotated into the direction of $P(\theta,\varphi)$ over the surface of a sphere. Since $P(\theta,\varphi)$ is available only in discrete directions, the integral is approximated by a sum:

$$\mathbf{I}^{\text{model}} = \frac{V}{2\pi}\left[\sum_i \sum_j \mathbf{R}^{-1}(\theta_i,\varphi_j)\mathbf{I}\mathbf{R}(\theta_i,\varphi_j)P(\theta_i,\varphi_j)A(\theta_i),\right]$$

V_n is the volume fraction of the mineral, $\mathbf{R}$ is the rotation matrix, θ and φ are the spherical coordinates, and A is the area of the surface element on the sphere defined by the measurement grid in a given direction. The principle deviatoric susceptibilities for calcite are ${}^{cc}I_1 = {}^{cc}I_2 = 0.37 \times 10^{-6}$ SI and ${}^{cc}I_3 = -0.73 \times 10^{-6}$ SI (Schmidt et al., 2006). Values for muscovite were determined from single crystals used in this study. Disregarding the anisotropy within the basal plane (see above), the values are ${}^{mu}I_1 = {}^{mu}I_2 = 5.9 \times 10^{-6}$ SI and ${}^{mu}I_3 = -11.8 \times 10^{-6}$ SI. For both minerals, the minimum susceptibility is along the c-axis.

3. Results

3.1. Texture

3.1.1. Calcite CPO

Calcite c-axes show a prolate CPO with the maximum oriented parallel to the compaction direction for all samples except the hand-pressed samples, which show the maximum at an angle to the compaction direction (Fig. 2, Table 2). The CPO intensity generally increases with increasing cold-press load, showing maxima from 1.2 multiples of random distribution (m.r.d.) to about 3.3 m.r.d., but this increase is not strictly monotonic. The texture strength, expressed by Δt, increases with compaction load (Fig. 3), and it is virtually independent of the muscovite content. Δt increases more at lower pressures and stabilizes above 200 MPa.

Except for the hand-pressed samples, the texture shapes are prolate with U always greater than 0.75, and greater than 0.90 in 20 of the 26 samples. The strongest calcite CPO is found in samples with 50% and 70% muscovite content.

3.1.2. Muscovite CPO

The pole figures of the muscovite c-axes generated from the (0 0 10) peaks are shown in Fig. 4, and the eigenvalues of the corresponding texture tensors are listed in Table 3. The c-axes have distributions that are always of prolate shape with the maximum parallel to the compaction direction (Fig. 4, Table 3). The ⟨1 1 0⟩ axes are homogeneously distributed in a girdle normal to the compaction direction. The contours in the pole figures of samples with only 5% or 10% muscovite are discrete and angular because of the small number of grains in each sample. For sample 5-200-2, the CPO intensity is abnormally high, which even results in negative eigenvalues of the texture tensor. The intensity of the texture generally increases with uniaxial cold-pressure; CPO maxima range between 3 and 5 m.r.d. at 20 MPa and between 5 and 9 m.r.d. at 200 MPa. The texture strength is dependent on the muscovite content, as for example it reaches a maximum for samples with 70% muscovite with $\Delta t = 0.57$. This texture strength would result in a paramagnetic AMS that reaches about 60% of the single crystal value. In general, the CPO of muscovite is much stronger than that of calcite.

3.2. Isothermal remanent magnetization (IRM)

The results from IRM acquisition experiments are partly described in Schmidt et al. (2008) and summarized in Table 4. In all samples, the magnetization is carried mainly by magnetite/maghemite. The samples with 10–70% muscovite are generally saturated below 800 mT and therefore could be entirely separated by high-field torque measurements. The remaining samples only partially saturated at 2 T, indicating the presence of hematite and/or goethite. The amount of high-coercivity phases was greatest in samples with 0% and 5% muscovite and very small in the pure muscovite samples. All samples show a significant anisotropy of isothermal remanent magnetization (AIRM) of 5–50%, which increases with muscovite content and indicates preferred orientation of ferromagnetic minerals. Since magnetite/maghemite is the only ferromagnetic mineral in samples with 30–70% muscovite content, it must show a shape-preferred orientation (SPO). As magnetite is assumed to be formed during hot isostatic pressing, its SPO cannot be induced by the uniaxial deformation, but may be created by the shape-preferred orientation of calcite and muscovite. The degree of AIRM increases with phyllosilicate content,

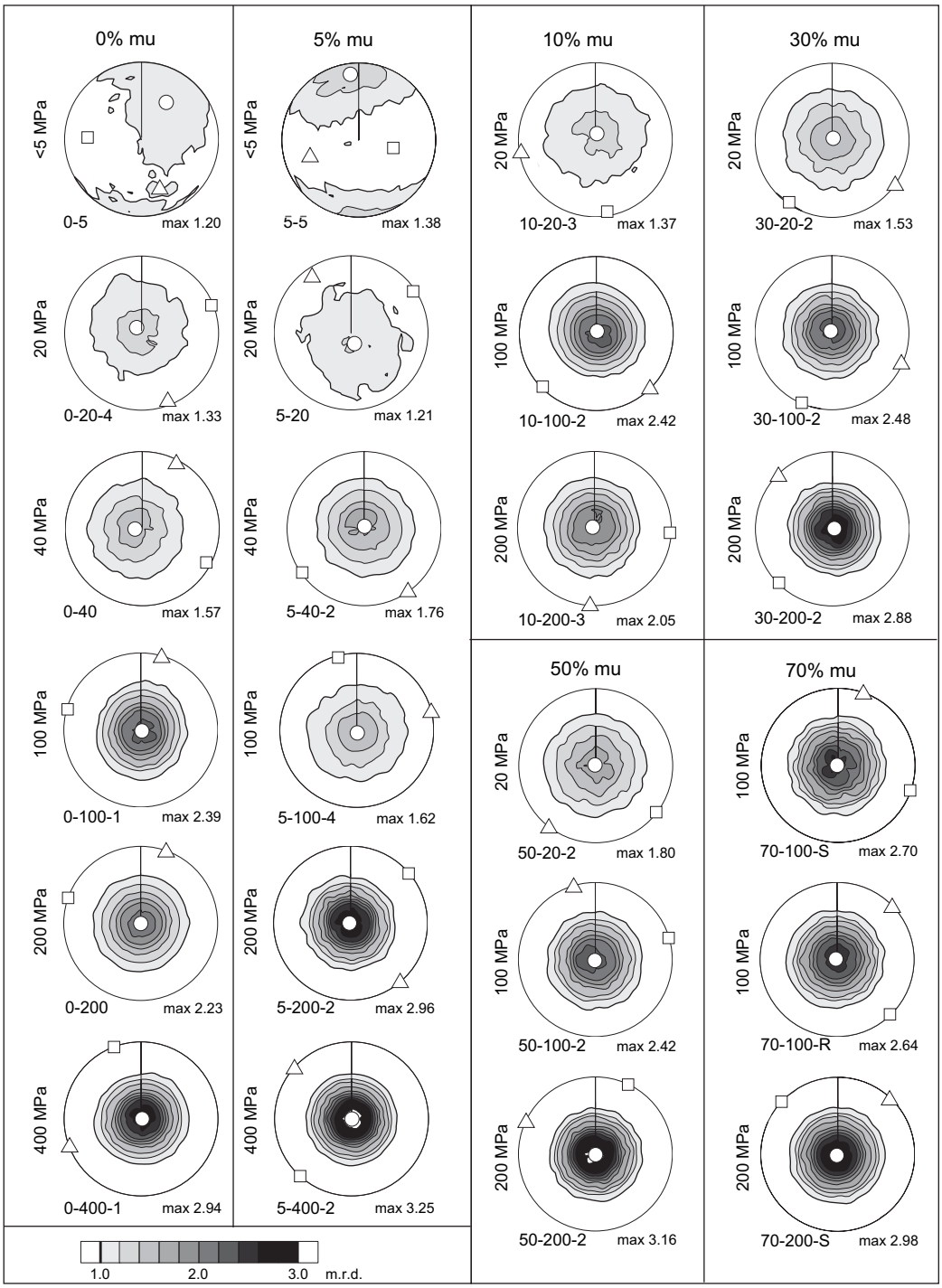

Fig. 2. Pole figures of the calcite *c*-axes (0 0 6) on lower hemisphere, equal-area projection. Contour lines are shown from 1 to 3 m.r.d. in an interval of 0.2 m.r.d., and maximum m.r.d. values are given in the lower right of each plot. Samples were compressed along the vertical axis (inclination 90°), which refers to the centers of the pole figure. The principal directions of the orientation tensor are indicated by open symbols. Squares, triangles and circles refer to minimum, intermediate and maximum values, respectively. 'mu' refers to the muscovite content in this and subsequent figures.

which implies that the SPO during the growth of magnetite is controlled by the orientation of the muscovite basal planes.

3.3. AMS

Since the porosities of the aggregates differ over a large range, the susceptibility was normalized by the mass of the specimens. The volumetric susceptibilities given were calculated using the crystal densities of 2.71 g/cm^3 for calcite and 2.82 g/cm^3 for muscovite.

3.3.1. Low-field and high-field AMS

The AMS measured in low fields is oblate with the minimum axis having inclinations $\geq$78° in all but the hand-pressed samples (Table 4), so that k_3 is parallel to the compression direction. The LF-AMS contains diamagnetic and paramagnetic contributions due to the CPO of calcite and muscovite as well as ferromagnetic contributions due to preferred orientation of ferrimagnetic and antiferromagnetic minerals detected by IRM acquisition. All three sub-fabrics have the same shape and

Table 2
Texture ellipsoids of the *c*-axis (0 0 6) for calcite (cc).

Specimen	CPO^{cc}_{max}	t_1^{cc}	D_1^{cc}	I_1^{cc}	t_2^{cc}	D_2^{cc}	I_2^{cc}	t_3^{cc}	D_3^{cc}	I_3^{cc}	Δt	U
0-5-0	1.20	0.351	33.8	41.9	0.333	159.4	33.0	0.316	271.9	30.5	0.035	0.00
0-20-4	1.33	0.363	317.8	82.2	0.320	158.7	7.3	0.317	68.3	2.7	0.046	−0.90
0-40-0	1.57	0.386	266.5	82.4	0.308	27.3	3.9	0.306	117.8	6.5	0.080	−0.95
0-100-1	2.39	0.462	133.3	88.5	0.275	15.8	0.7	0.263	285.8	1.3	0.199	−0.88
0-200-0	2.23	0.444	164.6	89.8	0.279	19.4	0.1	0.276	289.4	0.1	0.168	−0.96
0-400-1	2.94	0.495	88.9	88.9	0.257	249.4	1.0	0.248	339.4	0.4	0.247	−0.92
5-5-0	1.38	0.371	352.7	15.1	0.323	252.2	33.9	0.306	102.9	52	0.066	−0.46
5-20-0	1.21	0.354	162.7	78.1	0.325	325.6	11.4	0.321	56.3	3.4	0.033	−0.75
5-40-2	1.76	0.405	11.3	87.5	0.300	144.6	1.7	0.295	234.6	1.8	0.111	−0.90
5-100-4	1.62	0.389	169.3	87.2	0.307	75.7	0.2	0.304	345.6	2.8	0.085	−0.92
5-200-2	2.96	0.502	271.6	88.9	0.252	139.6	0.7	0.246	49.5	0.8	0.257	−0.95
5-400-2	3.25	0.522	116.1	89.5	0.241	311.9	0.4	0.237	221.9	0.1	0.285	−0.98
10-20-3	1.37	0.366	13.6	83.5	0.319	260.9	2.5	0.315	170.6	6.0	0.050	−0.85
10-100-2	2.42	0.463	20.1	87.4	0.274	135.2	1.1	0.263	225.3	2.3	0.200	−0.89
10-200-3	2.05	0.447	307.2	87.7	0.278	183.3	1.3	0.276	93.2	1.9	0.171	−0.97
30-20-2	1.53	0.393	29.9	87.6	0.304	124.8	0.2	0.303	214.8	2.4	0.090	−0.98
30-100-2	2.48	0.466	322.5	87.8	0.269	113.3	2.0	0.265	203.4	1.1	0.200	−0.97
30-200-2	2.88	0.503	80.4	87.9	0.252	314.9	1.2	0.245	224.8	1.7	0.258	−0.94
50-20A-2	1.80	0.417	311.5	88.9	0.294	217.5	0.1	0.290	127.5	1.1	0.127	−0.94
50-20B-S	1.71	0.404	159.4	88.0	0.299	60.2	0.3	0.297	330.2	2.0	0.107	−0.95
50-100A-2	2.42	0.473	206.6	88.9	0.265	343.6	0.8	0.262	73.6	0.8	0.211	−0.97
50-100B-S	2.82	0.495	133.1	88.2	0.255	1.7	1.2	0.250	271.7	1.4	0.246	−0.95
50-200A-2	3.16	0.527	162.5	89.3	0.238	295.3	0.5	0.234	25.3	0.5	0.293	−0.97
70-100-R	2.64	0.499	289.8	88.7	0.251	46.0	0.6	0.249	136.0	1.2	0.250	−0.98
70-100-0	2.70	0.502	274.3	88.9	0.249	19.2	0.3	0.249	109.2	1.1	0.253	−1.00
70-200-0	2.98	0.523	221.5	88.5	0.240	43.1	1.5	0.237	313.1	0.0	0.285	−0.98

CPO_{max} indicates pole figure maximum intensity; t_i are the texture eigenvalues; D_i and I_i are the corresponding declinations and inclinations in degree, $\Delta t = t_1 - t_3$ in this and subsequent Tables.

orientation, and their superposition generates the strong oblate AMS in the samples.

In Fig. 5, the dependency of the AMS on compaction and composition is illustrated for LF-AMS and HF-AMS, where any contribution due to magnetite/maghemite to the HF-AMS has been removed. The LF-AMS shows generally higher values, since it includes the ferrimagnetic contribution. It is dominated by the muscovite content, and a correlation of LF-AMS with compression is only observed in the muscovite-rich samples. This suggests that the LF-AMS is overprinted by a ferrimagnetic sub-fabric of varying strength. For example, the LF-AMS of samples with 70% muscovite is stronger than that for pure muscovite samples due to the stronger ferromagnetic sub-fabric indicated by a higher M_{rs} (Table 4). The HF-AMS shows an increase in magnitude with both compression and muscovite content. This comparison demonstrates that the separation of the ferrimagnetic AMS alone can improve the quality of AMS data of para/diamagnetic samples.

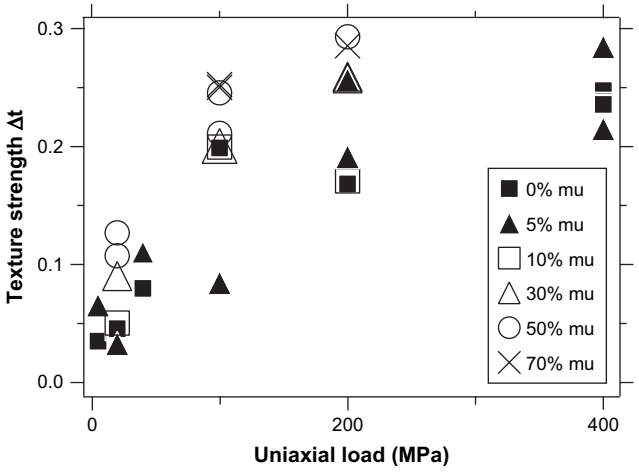

Fig. 3. Texture strength (Δt) of calcite *c*-axes versus load during cold-pressing.

3.3.2. Diamagnetic and paramagnetic AMS

The diamagnetic fabric could only be separated from samples with muscovite content between 5% and 30%. For greater muscovite content, the magnitude and the shape of the diamagnetic AMS ellipsoid become quite variable due to the measurement uncertainty. For this reason, the diamagnetic sub-fabric is not considered for samples with >30% muscovite content.

The results for the separated diamagnetic and paramagnetic deviatoric susceptibility tensors are listed in Tables 5 and 6. Note that the intensity of the diamagnetic and paramagnetic AMS is proportional to the content of the respective diamagnetic or paramagnetic mineral.

The diamagnetic fabrics are generally oblate with k_3 sub-parallel to the compression direction (inclination = 90°), except for samples with ≥50% muscovite content for which the diamagnetic fabric could not be isolated and sample 10-20-3, which has a very weak calcite CPO. The intensity of the diamagnetic AMS ranges between 3×10^{-8} SI and 3×10^{-7} SI. The maximum value of Δk for the pure calcite samples is considerably weaker than that of the axially deformed Carrara marble measured by Owens and Rutter (1978), who reported maximum values for Δk of 0.8×10^{-6} SI. The paramagnetic sub-fabrics are oblate for all samples with k_3 sub-parallel to the compression direction. The paramagnetic fabric is much stronger than the diamagnetic fabric. This is reflected in Δk, which is between 1×10^{-7} SI and 8×10^{-6} SI.

4. Discussion

4.1. Development of the CPO

The calcite and muscovite textures are generated by different deformation mechanisms. The calcite CPO is assumed to be created

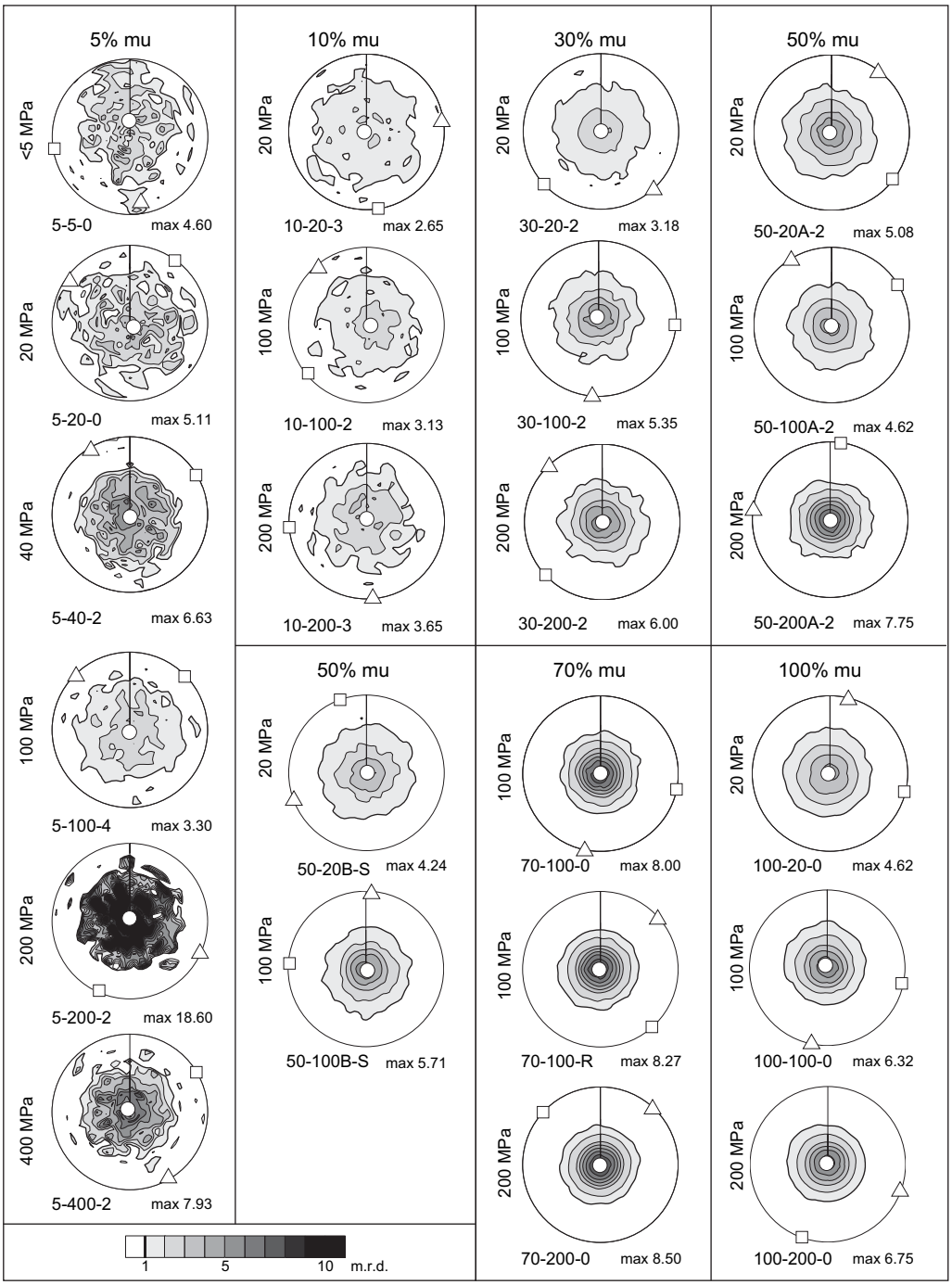

Fig. 4. Pole figures of the muscovite *c*-axes (0 0 10) on lower hemisphere, equal-area projection. Contour lines are shown from 1 to 10 m.r.d. in an interval of 1 m.r.d., and maximum m.r.d. values are given in the lower right of each plot. Samples were compressed along the vertical axis (inclination 90°), which refers to the centers of the pole figures. The principal directions of the orientation tensor are indicated by open symbols. Squares, triangles and circles refer to minimum, intermediate and maximum values, respectively.

mainly by twinning during cold-pressing, which rotates the *c*-axes towards the maximum shortening direction. A small contribution is also provided by the shape-preferred orientation of rhombohedra-shaped grains to the CPO (Schmidt et al., 2008). The subsequent hot isostatic pressing does not change the principal shape of the texture (e.g., Barnhoorn et al., 2005), however, slight changes in the intensity might occur. The non-monotonical increase in CPO intensity with increasing pressure could result from a switch of the main deformation mechanism or from imperfections induced during sample preparation. The deviation of the CPO maximum from the compaction direction in the hand-pressed samples 0-5-0 and 5-5-0 must be caused by non-isotropic deformation during annealing. Since these samples had a very high porosity after cold-pressing, they experienced further compaction during annealing, whereby the compaction was probably not fully isotropic. The calcite CPO maximum was rotated towards the new shortening direction (see also Rutter and Rusbridge, 1977), while the muscovite CPO was not affected.

The texture of the muscovite fraction results from rigid body rotation during compaction. The basal planes can easily rotate normal to the compression direction, which results in a strong *c*-axis CPO along the compression direction. The CPO is not much changed by subsequent glide on the basal plane and kinking.

Table 3
Texture ellipsoids of the *c*-axis from (0 0 10) peaks for muscovite (mu).

Specimen	CPO^{cc}_{max}	t_1^{mu}	D_1^{mu}	I_1^{mu}	t_2^{mu}	D_2^{mu}	I_2^{mu}	t_3^{mu}	D_3^{mu}	I_3^{mu}	Δt	U
5-5-0	4.60	0.553	356.6	73.2	0.289	170.5	16.7	0.158	261.0	1.7	0.395	−0.33
5-20-0	5.11	0.588	136.6	84.4	0.232	305.7	5.5	0.180	35.8	1.1	0.408	−0.75
5-40-2	6.63	0.830	175.2	87.5	0.114	329.2	2.3	0.056	59.3	1.1	0.774	−0.85
5-100-4	3.30	0.540	191.2	87.8	0.235	315.7	1.3	0.225	45.7	1.8	0.315	−0.94
5-200-2	18.60	1.503	353.2	86.9	−0.188	113.8	1.6	−0.315	203.8	2.7	1.818	−0.86
5-400-2	7.93	0.871	321.9	86.3	0.076	149.2	3.6	0.053	59.2	0.5	0.818	−0.94
10-20-3	2.65	0.459	269.1	87.6	0.272	81.2	2.4	0.269	171.3	0.3	0.191	−0.96
10-100-2	3.13	0.483	96.3	85.6	0.266	320.5	3.2	0.250	230.4	3.1	0.233	−0.86
10-200-3	3.65	0.558	356.7	87.5	0.225	175.4	2.5	0.217	265.4	0.1	0.341	−0.95
30-20-2	3.18	0.485	13.5	89.7	0.261	137.2	0.2	0.254	227.2	0.3	0.231	−0.94
30-100-2	5.35	0.584	317.7	87.7	0.209	184.7	1.6	0.207	94.7	1.7	0.376	−0.99
30-200-2	6.00	0.619	81.2	89.4	0.196	316.9	0.3	0.185	226.9	0.5	0.434	−0.95
50-20A-2	5.08	0.611	272.1	88	0.196	37.3	1.2	0.193	127.3	1.6	0.418	−0.98
50-20B-S	4.24	0.557	72.2	89.1	0.224	250.2	0.9	0.219	340.2	0	0.339	−0.97
50-100A-2	4.62	0.548	205.1	89.1	0.228	328.6	0.5	0.224	58.6	0.8	0.324	−0.98
50-100B-S	5.71	0.605	135.2	87.8	0.200	4.2	1.4	0.195	274.1	1.7	0.410	−0.98
50-200A-2	7.75	0.677	147.2	89.1	0.166	277.9	0.6	0.157	7.9	0.7	0.520	−0.97
70-100-R	8.27	0.714	259.3	88.6	0.146	48.2	1.2	0.140	138.2	0.7	0.574	−0.98
70-100-0	8.00	0.712	337	89.6	0.147	191.7	0.3	0.140	101.7	0.2	0.572	−0.98
70-200-0	8.50	0.712	219.1	89.3	0.147	42.5	0.7	0.141	312.5	0	0.571	−0.98
100-20-0	4.62	0.580	267.2	88.1	0.213	13.7	0.5	0.207	103.8	1.8	0.373	−0.97
100-100-0	6.32	0.612	325.1	86.8	0.195	191.9	2.2	0.193	101.8	2.3	0.420	−0.99
100-200-0	6.75	0.627	311.3	88.3	0.188	109.5	1.6	0.185	199.5	0.6	0.442	−0.99

Table 4
Results from low-field AMS measurements and IRM acquisition.

Specimen	Low-field measurements								IRM acquisition		
	k_M (SI)	l_1 (SI)	l_2 (SI)	l_3 (SI)	D_3	I_3	U	Δk (SI)	H_{rs} (mT)	M_{rs} (A/m)	M_c/M_a
0-5-0	−1.08E−05	1.51E−07	5.82E−08	−2.12E−07	275	59	0.49	3.62E−07	≫2500	4.6E−02	1.06
0-20-4	−9.42E−06	1.13E−07	5.75E−08	−1.72E−07	302	88	0.61	2.85E−07	>2500	1.1E−01	1.06
0-40-0	−1.05E−05	1.06E−07	−3.28E−09	−1.04E−07	164	88	−0.04	2.10E−07	>2500	9.5E−02	1.06
0-100-1	−9.22E−06	2.18E−07	1.54E−07	−3.84E−07	1	84	0.79	6.01E−07	2000	1.2E−01	1.07
0-200-0	−9.42E−06	1.44E−07	3.54E−08	−1.82E−07	140	86	0.33	3.27E−07	2250	1.2E−01	1.08
0-400-1	−9.08E−06	3.66E−07	2.03E−07	−5.98E−07	258	87	0.66	9.65E−07	2000	9.5E−02	1.16
5-5-0	−1.46E−06	7.58E−07	−4.53E−07	−8.61E−07	259	41	−0.50	1.62E−06			
5-20-0	−4.71E−06	1.56E−07	8.26E−08	−2.48E−07	348	83	0.64	4.05E−07	2500	1.2E−01	1.05
5-40-2	−2.33E−06	2.90E−07	9.86E−08	−4.49E−07	338	87	0.48	7.39E−07	2200	1.2E−01	1.04
5-100-4	−1.34E−06	1.82E−07	5.24E−08	−2.74E−07	300	80	0.43	4.56E−07	>2500	3.0E−01	1.05
5-200-2	1.06E−06	1.08E−06	5.56E−07	−1.63E−06	95	78	0.62	2.71E−06	>2500	2.4E−01	1.15
5-400-2	−3.68E−06	3.29E−07	2.60E−07	−6.67E−07	350	86	0.86	9.96E−07	2500	1.7E−01	1.13
10-20-3	1.03E−05	4.10E−07	1.42E−07	−5.29E−07	68	86	0.43	9.39E−07	1000	4.6E−01	1.04
10-100-2	8.34E−06	6.92E−07	4.65E−07	−1.16E−06	43	87	0.75	1.85E−06	1000	4.1E−01	1.14
10-200-3	1.09E−05	7.28E−07	4.01E−08	−7.68E−07	177	88	0.08	1.50E−06	500	4.6E−01	1.08
30-20-2	4.81E−05	1.71E−06	1.12E−06	−2.71E−06	121	89	0.73	4.42E−06	300	1.1E−00	1.13
30-100-2	4.55E−05	1.53E−06	1.38E−06	−2.90E−06	316	89	0.93	4.43E−06	500	1.1E−00	1.18
30-200-2	9.41E−05	3.13E−06	3.05E−06	−6.18E−06	329	89	0.98	9.31E−06	500	1.0E−00	1.20
50-20A-2	5.98E−05	2.20E−06	1.95E−06	−4.15E−06	340	88	0.92	6.35E−06	300	9.4E−01	1.17
50-20B-S	1.10E−04	2.75E−06	2.27E−06	−5.03E−06	208	90	0.88	7.78E−06	300	1.7E−00	1.20
50-100A-2	5.81E−05	2.58E−06	1.54E−06	−3.91E−06	245	89	0.68	6.48E−06	300	7.2E−01	1.22
50-100B-S	1.02E−04	2.69E−06	2.54E−06	−5.23E−06	308	87	0.96	7.93E−06	300	1.9E−00	1.24
50-200A-2	5.81E−05	2.69E−06	1.69E−06	−4.14E−06	258	89	0.71	6.83E−06	300	7.7E−01	1.25
50-200B-S	1.02E−04	3.02E−06	2.57E−06	−5.59E−06	283	87	0.90	8.60E−06	300	1.8E−00	1.30
70-20-0	9.79E−05	3.63E−06	2.94E−06	−6.58E−06	47	89	0.86	1.02E−05	350	1.3E−00	1.15
70-100-0	9.94E−05	3.49E−06	3.31E−06	−6.80E−06	180	89	0.97	1.03E−05	–	–	–
70-100-R	1.01E−04	3.40E−06	3.31E−06	−6.70E−06	157	89	0.98	1.01E−05	–	–	–
70-200-0	9.47E−05	3.49E−06	3.08E−06	−6.57E−06	248	88	0.92	1.01E−05	500	1.1E−00	1.36
100-20-0	1.02E−04	2.48E−06	2.16E−06	−4.64E−06	220	89	0.91	7.11E−06	2500	1.2E−02	–
100-100-0	1.02E−04	2.84E−06	2.68E−06	−5.51E−06	198	88	0.96	8.35E−06	≫2500	1.4E−02	1.49
100-200-0	1.02E−04	2.90E−06	2.79E−06	−5.69E−06	219	89	0.98	8.59E−06	2500	9.3E−03	1.60

l_i are the eigenvalues of the deviatoric susceptibility tensor **I**; D_i and I_i are the declination and inclination of the eigenvectors; and U is the shape parameter. Compression direction was at an inclination of 90°. H_{rs} is the saturation field of remanence, M_{rs} the remanent magnetization at 2.5 T; and M_c/M_a is the ratio of M_{rs} along and normal to the compression axis and indicates the degree of anisotropy of IRM.

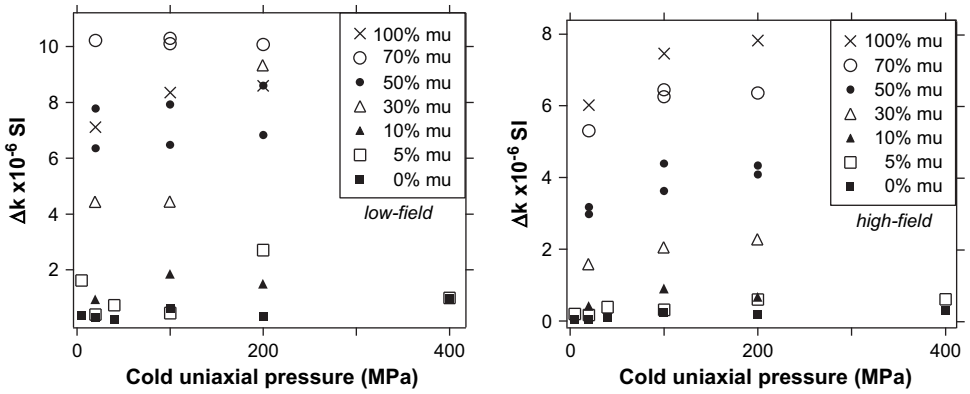

Fig. 5. Low-field (left) and para/diamagnetic high-field AMS (right) of all samples illustrating their dependence on muscovite (mu) content and load during compaction. Note the different vertical scales.

4.2. Correlation of AMS and CPO

4.2.1. Correlation of diamagnetic sub-fabric and calcite CPO

For the pure calcite samples, measured and modeled diamagnetic AMS agree very well in intensity, shape and direction (Table 5, Fig. 6). Note that the diamagnetic AMS is linearly proportional to calcite content, such that for a pure calcite sample with perfect alignment of all *c*-axes ($\Delta t = 1.0$), Δk would result in the single crystal value of 1.10×10^{-6} SI. Differences in the eigenvalues are within the uncertainty range. Sample 0-5 is the only sample in which the principal directions of the AMS and texture ellipsoids do not agree with one another, due to the very weak AMS, which is at the sensitivity limit of the torque magnetometer. The high-coercivity ferromagnetic phases in the samples do not affect the anisotropy, which suggests, that they are randomly oriented in the pure calcite samples.

For the 95%-calcite samples, the measured tensors agree well in shape and magnitude with the modeled ones, even for samples with weak texture. The deviations from the modeled values are within the uncertainty range for all samples, except for sample 5-200-2. The presence of muscovite is assumed to influence the alignment of high-coercivity phases such as goethite and hematite (Table 4), which may explain the slight deviations of the measured AMS towards larger values. This effect is absent in the pure calcite samples. For sample 5-200-2, the contribution of hematite was corrected by using the method of Martín-Hernández and Hirt (2004). Δk of the resultant tensor (5-200-2h in Table 5) agrees better with the modeled value, but its shape is distorted. However, this result confirms the contribution of hematite to the larger measured values.

The tensors of the samples with 90 and 70% calcite agree very well with the modeled tensors. Larger deviations in AMS shape from the theoretical values are observed for the samples cold-pressed at 20 MPa. High-coercivity contributions cannot affect the result, as the samples saturate below 1 T (Table 4).

4.2.2. Correlation of paramagnetic sub-fabric and muscovite CPO

The modeled and the measured paramagnetic deviatoric tensors are characterized by nearly perfectly oblate AMS ellipsoids with the axis of the minimum eigenvalues close to the compression

Table 5
Parameters of the diamagnetic deviatoric susceptibility tensor **l** from high-field measurements and modeled from calcite *c*-axis pole figures.

Specimen	Measured diamagnetic tensor											Modeled diamagnetic tensor						
	l_1	D_1	I_1	l_2	D_2	I_2	l_3	D_3	I_3	U	Δk	l_1	l_2	l_3	D_3	I_3	U	Δk
0-5-0	1.55E−08	354	5	1.88E−09	264	5	−1.73E−08	127	83	0.17	3.28E−08	1.93E−08	1.49E−11	−1.93E−08	34	42	0.00	3.86E−08
0-20-4	1.92E−08	263	1	1.76E−08	353	1	−3.68E−08	136	89	0.94	5.61E−08	1.76E−08	1.50E−08	−3.26E−08	318	82	0.90	5.02E−08
0-40-0	3.04E−08	316	2	2.57E−08	46	6	−5.62E−08	205	84	0.89	8.66E−08	3.00E−08	2.77E−08	−5.78E−08	267	82	0.95	8.78E−08
0-100-1	8.63E−08	161	1	7.35E−08	251	0	−1.59E−07	360	89	0.90	2.46E−07	7.71E−08	6.44E−08	−1.42E−07	133	89	0.88	2.19E−07
0-200-0	6.51E−08	146	4	5.86E−08	55	2	−1.23E−07	294	86	0.93	1.89E−07	6.29E−08	5.93E−08	−1.22E−07	165	90	0.96	1.85E−07
0-400-1	1.00E−07	290	0	8.59E−08	20	0	−1.86E−07	157	90	0.90	2.86E−07	9.41E−08	8.39E−08	−1.78E−07	89	89	0.92	2.72E−07
5-5-0	2.75E−08	144	6	1.69E−08	41	63	−4.44E−08	237	26	0.70	7.19E−08	2.89E−08	1.06E−08	−3.95E−08	353	15	0.46	6.85E−08
5-20-0	3.27E−08	105	14	1.13E−08	197	10	−4.39E−08	320	73	0.44	7.66E−08	1.29E−08	8.59E−09	−2.15E−08	163	78	0.75	3.44E−08
5-40-2	4.25E−08	106	9	3.32E−08	15	4	−7.57E−08	263	80	0.84	1.18E−07	4.05E−08	3.48E−08	−7.54E−08	11	88	0.90	1.16E−07
5-100-4	4.29E−08	53	1	2.42E−08	143	2	−6.70E−08	289	87	0.66	1.10E−07	3.06E−08	2.72E−08	−5.78E−08	169	87	0.92	8.84E−08
5-200-2	1.27E−07	223	2	9.96E−08	313	8	−2.26E−07	117	82	0.85	3.53E−07	9.17E−08	8.47E−08	−1.76E−07	272	89	0.95	2.68E−07
5-200-2h	1.09E−07	–	–	3.64E−08	–	–	−1.45E−07	241	68	0.43	2.54E−07	9.17E−08	8.47E−08	−1.76E−07	272	89	0.95	2.68E−07
5-400-2	1.17E−07	99	0	1.13E−07	9	1	−2.31E−07	207	89	0.98	3.48E−07	1.00E−07	9.68E−08	−1.97E−07	116	90	0.98	2.98E−07
10-20-3	3.96E−08	126	14	−9.38E−09	222	23	−3.02E−08	8	63	−0.40	6.98E−08	1.79E−08	1.41E−08	−3.20E−08	14	84	0.85	4.99E−08
10-100-2	7.33E−08	207	0	4.75E−08	117	2	−1.21E−07	302	88	0.73	1.94E−07	6.95E−08	5.85E−08	−1.28E−07	20	87	0.89	1.98E−07
10-200-3	5.63E−08	282	6	3.62E−08	192	3	−9.25E−08	78	84	0.73	1.49E−07	5.72E−08	5.48E−08	−1.12E−07	307	88	0.97	1.69E−07
30-20-2	3.69E−08	82	0	1.42E−08	352	13	−5.12E−08	173	77	0.49	8.81E−08	2.33E−08	2.28E−08	−4.61E−08	30	88	0.98	6.94E−08
30-100-2	5.51E−08	133	2	4.76E−08	43	6	−1.03E−07	241	84	0.91	1.58E−07	5.22E−08	4.98E−08	−1.02E−07	323	88	0.97	1.54E−07
30-200-2	6.61E−08	50	1	5.40E−08	140	3	−1.20E−07	297	87	0.87	1.86E−07	6.84E−08	6.29E−08	−1.31E−07	80	88	0.94	2.00E−07

l_i are the eigenvalues of **l**, D_i and I_i are the declination and inclination of the eigenvectors, and U is the shape parameter. Compression direction was at an inclination of 90°. Principal axes of the modeled AMS ellipsoids are coaxial with those of the texture ellipsoids, whereby the direction of l_1 corresponds to t_3, and l_3 and corresponds to t_1 in this and Table 6. 5-200-2h indicates the values of 5-200-2 after the separation of the hematite contribution. The modeled values have been re-calculated for the respective calcite content.

Table 6
Parameters of the paramagnetic deviatoric susceptibility tensor **I** from high-field measurements and modeled from muscovite c-axis pole figures (0 0 10).

Specimen	Measured Paramagnetic tensor											Modeled Paramagnetic tensor						
	I_1	D_1	I_1	I_2	D_2	I_2	I_3	D_3	I_3	U	Δk	I_1	I_2	I_3	D_3	I_3	U	Δk
5-5-0	9.44E−08	190	7	4.57E−09	283	23	−9.90E−08	84	66	0.07	1.93E−07	3.11E−06	7.76E−07	−3.88E−06	357	73	0.33	6.99E−06
5-20-0	5.95E−08	10	4	2.63E−08	100	2	−8.57E−08	218	85	0.52	1.09E−07	2.71E−06	1.80E−06	−4.51E−06	137	84	0.75	7.22E−06
5-40-2	9.31E−08	192	2	6.44E−08	282	3	−1.57E−07	68	87	0.77	2.51E−07	4.91E−06	3.88E−06	−8.79E−06	175	88	0.85	1.37E−05
5-100-4	8.07E−08	133	9	4.70E−08	42	5	−1.28E−07	280	80	0.68	2.08E−07	1.92E−06	1.74E−06	−3.66E−06	191	88	0.94	5.58E−06
5-200-2	7.80E−08	336	1	6.13E−08	246	0	−1.39E−07	145	89	0.85	2.17E−07	1.15E−05	9.23E−06	−2.07E−05	353	87	0.86	3.22E−05
5-400-2	8.30E−08	171	1	7.63E−08	261	3	−1.59E−07	71	87	0.94	2.42E−07	4.97E−06	4.55E−06	−9.52E−06	322	86	0.94	1.45E−05
10-20-3	1.23E−07	34	1	1.02E−07	304	8	−2.25E−07	130	82	0.88	3.48E−07	1.15E−06	1.08E−06	−2.23E−06	269	88	0.96	3.37E−06
10-100-2	2.32E−07	242	1	2.10E−07	152	2	−4.42E−07	354	88	0.93	6.74E−07	1.47E−06	1.18E−06	−2.66E−06	96	86	0.86	4.13E−06
10-200-3	1.82E−07	7	3	1.52E−07	277	1	−3.34E−07	162	87	0.88	5.17E−07	2.06E−06	1.92E−06	−3.98E−06	357	88	0.95	6.04E−06
30-20-2	4.98E−07	11	1	4.81E−07	281	1	−9.79E−07	129	89	0.98	1.48E−06	1.40E−06	1.28E−06	−2.68E−06	14	90	0.94	4.08E−06
30-100-2	6.40E−07	225	1	6.07E−07	315	1	−1.25E−06	104	89	0.97	1.89E−06	2.23E−06	2.20E−06	−4.43E−06	318	88	0.99	6.66E−06
30-200-2	6.86E−07	26	0	6.36E−07	296	0	−1.32E−06	159	90	0.95	2.01E−06	2.62E−06	2.43E−06	−5.05E−06	81	89	0.95	7.68E−06
50-20A-2	9.83E−07	180	1	9.27E−07	270	1	−1.91E−06	46	89	0.96	2.89E−06	2.49E−06	2.43E−06	−4.91E−06	272	88	0.98	7.40E−06
50-20B-S	1.09E−06	140	1	9.75E−07	50	0	−2.07E−06	311	89	0.93	3.16E−06	2.03E−06	1.94E−06	−3.97E−06	72	89	0.97	6.00E−06
50-100A-2	1.24E−06	27	1	1.13E−06	297	0	−2.37E−06	194	89	0.94	3.61E−06	1.93E−06	1.87E−06	−3.80E−06	205	89	0.98	5.73E−06
50-100B-S	1.48E−06	193	2	1.41E−06	103	1	−2.88E−06	353	88	0.97	4.36E−06	2.45E−06	2.36E−06	−4.80E−06	135	88	0.98	7.25E−06
50-200A-2	1.33E−06	39	0	1.30E−06	309	1	−2.63E−06	154	89	0.99	3.97E−06	3.11E−06	2.97E−06	−6.08E−06	147	89	0.97	9.20E−06
50-200B-S	1.44E−06	73	1	1.41E−06	163	2	−2.85E−06	326	88	0.98	4.30E−06	–	–	–	–	–	–	–
70-20-0[a]	1.79E−06	353	0	1.74E−06	263	1	−3.51E−06	93	89	0.98	5.30E−06	–	–	–	–	–	–	–
70-100-0	2.09E−06	49	0	2.05E−06	319	2	−4.14E−06	145	89	0.98	6.24E−06	3.42E−06	3.29E−06	−6.71E−06	337	90	0.98	1.01E−05
70-100-R	2.16E−06	312	1	2.07E−06	42	0	−4.22E−06	135	89	0.97	6.38E−06	3.41E−06	3.32E−06	−6.74E−06	259	89	0.98	1.02E−05
70-200-0	2.11E−06	347	0	2.07E−06	77	0	−4.18E−06	221	90	0.99	6.29E−06	3.40E−06	3.30E−06	−6.70E−06	219	89	0.98	1.01E−05
100-20-0	1.99E−06	358	1	1.91E−06	88	1	−3.91E−06	201	89	0.97	5.90E−06	2.23E−06	2.13E−06	−4.36E−06	267	88	0.97	6.60E−06
100-100-0	2.46E−06	336	1	2.44E−06	67	1	−4.90E−06	179	89	1.00	7.36E−06	2.49E−06	2.45E−06	−4.94E−06	325	87	0.99	7.43E−06
100-200-0	2.57E−06	19	1	2.50E−06	289	1	−5.07E−06	162	89	0.98	7.64E−06	2.62E−06	2.58E−06	−5.20E−06	311	88	0.99	7.82E−06

[a] Values of 70-20-0 include diamagnetic AMS, whereas this makes up about 1%.

direction of 90° inclination (Table 6). The measured AMS agrees very well with the modeled AMS in shape (U-parameter) and orientation (Fig. 7). The straight lines show the theoretical paramagnetic AMS at a given Δt for the respective muscovite contents. In general, the modeled and measured values agree well. An almost perfect agreement is observed for the 100% muscovite samples. For samples with 10% and 30% muscovite, the agreement is of similar quality. For 70% muscovite content, the values of Δk are systematically too low or the values for Δt are too high, respectively. At 50% muscovite, the correlation is poor, although the AMS measurements are assumed to be very reliable for such high muscovite content.

The deviations between modeled and measured values in samples with ≥50% muscovite cannot be due to the uncertainty of

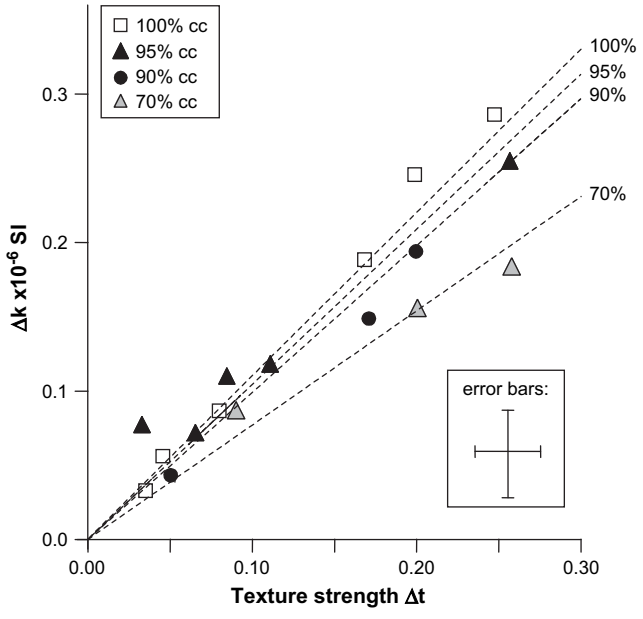

Fig. 6. Diamagnetic susceptibility difference Δk versus texture strength parameter Δt for different calcite contents. Straight lines show the theoretical values of Δk for the respective calcite contents. Error bars in inset are valid for every data point, in which the error bar for Δt is estimated from the comparative study of Wenk (1991), and the error bar for Δk indicates the uncertainty of the torque magnetometer.

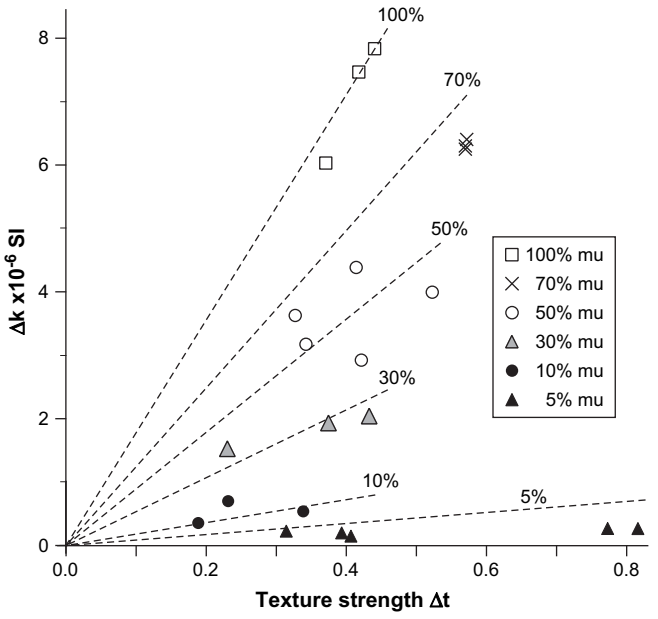

Fig. 7. Paramagnetic susceptibility difference Δk versus muscovite texture strength parameter Δt for different muscovite content. Straight lines show the theoretical values of Δk for the respective muscovite content.

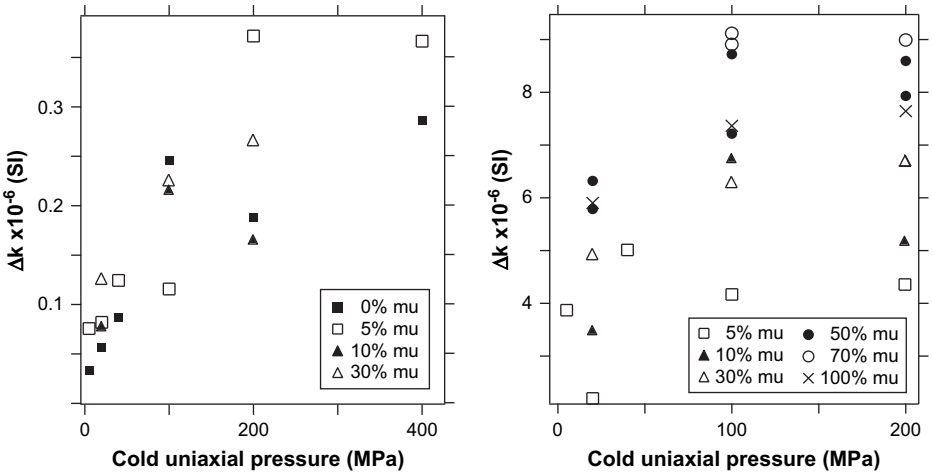

Fig. 8. (Left) Diamagnetic AMS versus compaction load for samples with different muscovite content. Δ*k* of two-phase samples is re-calculated for 100% calcite content. (Right) Paramagnetic AMS versus compaction load for samples with different muscovite content. Δ*k* of two-phase samples is re-calculated for 100% muscovite content.

the AMS measurement or the separation of diamagnetic and paramagnetic sub-fabric. This leads us to the assumption, that the CPO intensities are incorrect. Overlapping of muscovite and calcite peaks may have led to an incorrect intensity of the pole figures, since for the pure muscovite samples the CPO agrees with the AMS. For samples with $\leq$30% muscovite content, the uncertainty in AMS may also contribute to the deviations between measured and modeled AMS. However, for the 5% muscovite samples, the deviations arise from imprecision in determining the (0 0 10) pole figures, due to small concentration.

4.3. Correlation of AMS and compaction

The relationship of AMS and compaction is an indirect one that is based on the correlation of CPO and compaction (Fig. 3, Tables 2 and 3). Δ*k* generally increases with compactional stress for both the diamagnetic and the paramagnetic sub-fabric (Fig. 8). To compare the values for samples with different composition, the values for the two-phase samples were normalized by recalculating the values of Δ*k* for 100% calcite or muscovite content, respectively. The strength of the diamagnetic anisotropy generally increases with compactional stress and is not significantly influenced by the muscovite content. The paramagnetic anisotropy is governed both by the compactional stress and the muscovite content. Fig. 8 also shows that the paramagnetic fabric relative to the muscovite content is strongest for samples containing 70% muscovite. This result is a direct effect of the better alignment of muscovite in these samples. In general, the diamagnetic sub-fabric is a more adequate indicator of compaction in calcite–muscovite rocks, since it is less dependent on the muscovite content than the paramagnetic sub-fabric.

5. Conclusions

The diamagnetic sub-fabric of synthetic calcite–muscovite aggregates was successfully isolated for samples with muscovite contents up to 30% and for cold-pressing by more than 20 MPa.

For pure calcite samples, the AMS modeled from the calcite CPO and the measured AMS agree very well, if no unsaturated ferromagnetic minerals affect the AMS. This result shows that the AMS is purely due to the CPO of calcite, and not influenced by grain boundaries, pore space, or other rocks properties. For the two-phase samples with up to 30% muscovite content and cold-pressed $>$20 MPa, very good agreement exists between the calcite CPO and the diamagnetic sub-fabric. For samples with very weak CPO, the intensity of the measured AMS agrees quite well with the modeled AMS, but deviates in shape and direction. The presence of ferromagnetic minerals with high coercivity can affect the measurements of the diamagnetic fabric. In conclusion, the diamagnetic AMS is a robust quantitative anisotropy parameter for calcite textures in rocks with up to 30% muscovite.

For the paramagnetic fraction, AMS reflects the muscovite CPO very well in all samples. The agreement with the modeled values from the (0 0 10) pole figure is very good in shape and orientation. Deviations in the intensity are assumed to result from large uncertainties in the intensity of the muscovite pole figures. The paramagnetic anisotropy is a valid tool to characterize muscovite textures in multiphase-rocks, if the paramagnetic AMS is carried by this mineral. The paramagnetic anisotropy as a fundamental physical parameter of rocks could serve as an independent parameter for the quantitative comparison of pole figures, since a quantitative comparison between neutron and X-ray diffraction as well as EBSD and *U*-stage is not easily achieved (Ullemeyer et al., 2000). In principal, the AMS method is not limited by a penetration depth, and the intensity of the paramagnetic fabric is linearly dependent on the muscovite content and the single crystal anisotropy.

In rocks, where the CPO increases with compaction, AMS is a reliable measure of compaction. Because diffraction methods are technically more laborious and can suffer from peak overlapping and penetration limits, the AMS method could be a practical method for the texture characterization of large sample sets. AMS is quickly measured and always represents the whole sample volume. However, the AMS intensity is related to the volume fraction of the mineral that is source of the AMS. Therefore, the approximate mineralogical composition of each sample should be known. Moreover, AMS only reflects the *c*-axis direction distributions for minerals with a uniaxial anisotropy. A thorough investigation of deformation processes, however, requires the complete CPO. Consequently, AMS measurements cannot replace texture measurements using diffraction methods. Yet a combination of AMS and diffraction methods assists the effectiveness of textural investigations on a regional scale.

Acknowledgements

The authors thank two anonymous reviewers and W. Dunn for their helpful comments. This work was supported by the Swiss National Science Foundation, Project no. 2-77646-05. BL

appreciates financial support by the German Federal Ministry of Education and Research (03-DU03-G3). Ekkehard Jansen's support with the neutron texture measurements and processing is greatly acknowledged.

References

Bailey, S.W., 1984. Classification and structures of the micas. In: Bailey, S.W. (Ed.), Micas. Reviews in Mineralogy, vol. 13. Mineralogical Society of America, Washington D.C., pp. 1–12.

Ballet, O., Coey, J.M.D., 1982. Magnetic properties of sheet silicates; 2:1 layer minerals. Physics and Chemistry of Minerals 8, 218–229.

Barnhoorn, A., Bystricky, M., Burlini, L., Kunze, K., 2005. Post-deformational annealing of calcite rocks. Tectonophysics 403, 167–191.

Bergmüller, F., Bärlocher, C., Geyer, B., Grieder, M., Heller, F., Zweifel, P., 1994. A torque magnetometer for measurements of the high-field anisotropy of rocks and crystals. Measurement Science and Technology 5, 1466–1470.

Bestmann, M., Kunze, K., Matthews, A., 2000. Evolution of a calcite marble shear zone complex on Thassos Island, Greece: microstructural and textural fabrics and their kinematic significance. Journal of Structural Geology 22, 1789–1807.

Borradaile, G.J., 1988. Magnetic susceptibility, petrofabrics, and strain: a review. Tectonophysics 156, 1–20.

Borradaile, G.J., Henry, B., 1997. Tectonic applications of magnetic susceptibility and its anisotropy. Earth-Science Reviews 42, 49–93.

Borradaile, G.J., Werner, T., 1994. Magnetic anisotropy of some phyllosilicates. Tectonophysics 235, 223–248.

Chadima, M., Hansen, A., Hirt, A.M., Hrouda, F., Siemes, H., 2004. Phyllosilicate preferred orientation as a control of magnetic fabric: evidence from neutron texture goniometry and low and high-field magnetic anisotropy (SE Rhenohercynian Zone of Bohemian Massif). In: Martín-Hernández, F., Lüneburg, C.M., Aubourg, C., Jackson, M. (Eds.), Magnetic Fabric: Methods and Applications. The Geological Society, London, Special Publications, vol. 238, pp. 361–380.

Cheeney, R.F., 1983. Statistical Methods in Geology for Field and Lab Decisions. Allen & Unwin, London.

Cifelli, F., Mattei, M., Chadima, M., Hirt, A.M., Hansen, A., 2005. The origin of tectonic lineation in extensional basins: combined neutron texture and magnetic analyses on "undeformed" clays. Earth and Planetary Science Letters 235, 62–78.

Coward, M.P., Whalley, J.S., 1979. Texture and fabric studies across the Kishorn Nappe, near Kyle of Lochalsh, Western Scotland. Journal of Structural Geology 1, 259–273.

Evans, M.A., Lewchuk, M.T., Elmore, R.D., 2003. Strain partitioning of deformation mechanisms in limestones: examining the relationship of strain and anisotropy of magnetic susceptibility (AMS). Journal of Structural Geology 25, 1525–1549.

Gehring, A.U., Fry, I.V., Luster, J., Sposito, G., 1993. Vanadium (IV) in a multimineral lateritic saprolite – a thermoanalytical and spectroscopic study. Soil Science Society of America Journal 57, 868–873.

Graham, J.W., 1954. Magnetic susceptibility anisotropy, an unexploited petrofabric element. Geological Society of America Bulletin 65, 1257–1258.

Hirt, A.M., Evans, K.F., Engelder, T., 1995. Correlation between magnetic-anisotropy and fabric for Devonian shales on the Appalachian Plateau. Tectonophysics 247, 121–132.

Hirt, A.M., Lowrie, W., Lüneburg, C.M., Lebit, H., Engelder, T., 2004. Magnetic and mineral fabric development in the Ordovician Martinsburg Formation in the Central Appalachian Fold and Thrust Belt, Pennsylvania. In: Martín-Hernández, F., Lüneburg, C.M., Aubourg, C., Jackson, M. (Eds.), Magnetic Fabric – Methods and Applications. The Geological Society, London, Special Publications, vol. 238, pp. 109–126.

Hrouda, F., 1982. Magnetic-anisotropy of rocks and its application in geology and geophysics. Geophysical Surveys 5, 37–82.

Hrouda, F., Schulmann, K., Suppes, M., Ullemayer, K., de Wall, H., Weber, K., 1997. Quantitive relationship between low-field AMS and phyllosilicate fabric: a review. Physics and Chemistry of the Earth 22, 153–156.

Ihmlé, P.F., Hirt, A.M., Lowrie, W., Dietrich, D., 1989. Inverse magnetic fabric in deformed limestones of the Morcles Nappe, Switzerland. Geophysical Research Letters 16, 1383–1386.

Jackson, M., 1990. Magnetic anisotropy of the Trenton limestone revisited. Geophysical Research Letters 17, 1121–1124.

Jansen, E., Schafer, W., Kirfel, A., 2000. The Jülich neutron diffractometer and data processing in rock texture investigations. Journal of Structural Geology 22, 1559–1564.

Jelinek, V., 1981. Characterization of the magnetic fabric of rocks. Tectonophysics 79, T63–T67.

Jelinek, V., 1985. The physical principles of measuring magnetic anisotropy with the torque magnetometer. Travaux Géophysiques 33, 177–198.

Kligfield, R., Lowrie, W., Hirt, A., Siddans, A.W.B., 1983. Effect of progressive deformation on remanent magnetization of Permian redbeds from the Alpes Maritimes (France). Tectonophysics 98, 59–85.

Lafrance, B., White, J.C., Williams, P.F., 1994. Natural calcite *c*-axis fabrics – an alternate interpretation. Tectonophysics 229, 1–18.

Lagroix, F., Borradaile, G.J., 2000. Tectonics of the circum-Troodos sedimentary cover of Cyprus, from rock magnetic and structural observations. Journal of Structural Geology 22, 453–469.

Leiss, B., Molli, G., 2003. 'High-temperature' texture in naturally deformed Carrara marble from the Alpi Apuane, Italy. Journal of Structural Geology 25, 649–658.

Lowrie, W., Hirt, A.M., 1987. Anisotropy of magnetic susceptibility in the Scaglia Rossa pelagic limestone. Earth Planetary Science Letters 55, 181–189.

Lüneburg, C.M., Lampert, S.A., Lebit, H.D., Hirt, A.M., Casey, M., Lowrie, W., 1999. Magnetic anisotropy, rock fabrics and finite strain in deformed sediments of SW Sardinia (Italy). Tectonophysics 307, 51–74.

Martin-Hernandez, F., Ferré, E.C., 2007. Separation of paramagnetic and ferrimagnetic anisotropies: a review. Journal of Geophysical Research: Solid Earth 112, B03105.

Martín-Hernández, F., Hirt, A.M., 2001. Separation of ferrimagnetic and paramagnetic anisotropies using a high-field torsion magnetometer. Tectonophysics 337, 209–221.

Martín-Hernández, F., Hirt, A.M., 2003. The anisotropy of magnetic susceptibility in biotite, muscovite and chlorite single crystals. Tectonophysics 367, 13–28.

Martín-Hernández, F., Hirt, A.M., 2004. A method for the separation of paramagnetic, ferrimagnetic and haematite magnetic subfabrics using high-field torque magnetometry. Geophysical Journal International 157, 117–127.

Martín-Hernández, F., Kunze, K., Julivert, M., Hirt, A.M., 2005. Mathematical simulations of anisotropy of magnetic susceptibility on composite fabrics. Journal of Geophysical Research B 110.

Owens, W.H., 1974. Mathematical model studies on factors affecting the magnetic anisotropy of deformed rocks. Tectonophysics 24, 115–131.

Owens, W.H., Bamford, D., 1976. Magnetic, seismic, and other anisotropic properties of rock fabrics. Philosophical Transactions of the Royal Society of London, Series A 283, 55–68.

Owens, W.H., Rutter, E.H., 1978. Development of magnetic-susceptibility anisotropy through crystallographic preferred orientation in a calcite rock. Physics of the Earth and Planetary Interiors 16, 215–222.

Piper, J.D.A., Mesci, L.B., Gursoy, H., Tatar, O., Davies, C.J., 2007. Palaeomagnetic and rock magnetic properties of travertine: its potential as a recorder of geomagnetic palaeosecular variation, environmental change and earthquake activity in the Sicak Cermik geothermal field, Turkey. Physics of the Earth and Planetary Interiors 161, 50–73.

Ratschbacher, L., Wenk, H.R., Sintubin, M., 1991. Calcite textures – examples from nappes with strain-path partitioning. Journal of Structural Geology 13, 369–384.

Rochette, P., 1988. Inverse magnetic fabric in carbonate-bearing rocks. Earth and Planetary Science Letters 90, 229–237.

Rochette, P., Vialon, P., 1984. Development of planar and linear fabrics in Dauphinois shales and slates (French Alps) studied by magnetic-anisotropy and its mineralogical control. Journal of Structural Geology 6, 33–38.

Rutter, E.H., Casey, M., Burlini, L., 1994. Preferred crystallographic orientation development during the plastic and superplastic flow of calcite rocks. Journal of Structural Geology 16, 1431–1446.

Rutter, E.H., Rusbridge, M., 1977. The effect of non-coaxial strain paths on crystallographic preferred orientation development in the experimental deformation of a marble. Tectonophysics 39, 73–86.

Schmidt, V., Burlini, L., Hirt, A.M., Leiss, B., 2008. Fabrication of synthetic calcite–muscovite rocks with variable texture – an analogue to cataclastic fabrics? Tectonophysics 449, 105–119.

Schmidt, V., Günther, D., Hirt, A.M., 2006. Magnetic anisotropy of calcite at room-temperature. Tectonophysics 418, 63–73.

Schmidt, V., Hirt, A.M., Hametner, K., Günther, D., 2007a. Magnetic anisotropy of carbonate minerals at room temperature and 77 K. American Mineralogist 92, 1673–1684.

Schmidt, V., Hirt, A.M., Rosselli, P., Martín-Hernández, F., 2007b. Separation of diamagnetic and paramagnetic anisotropy by high-field, low-temperature torque measurements. Geophysical Journal International 168, 40–47.

Siegesmund, S., Ullemeyer, K., Dahms, M., 1995. Control of magnetic rock fabrics by mica preferred orientation – a quantitative approach. Journal of Structural Geology 17, 1601–1613.

Trullenque, G., Kunze, K., Heilbronner, R., Stunitz, H., Schmid, S.M., 2006. Microfabrics of calcite ultramylonites as records of coaxial and non-coaxial deformation kinematics: examples from the Rocher de l'Yret shear zone (Western Alps). Tectonophysics 424, 69–97.

Ullemeyer, K., Braun, G., Dahms, M., Kruhl, J.H., Olesen, N.O., Siegesmund, S., 2000. Texture analysis of a muscovite-bearing quartzite: a comparison of some currently used techniques. Journal of Structural Geology 22, 1541–1557.

Uyeda, S., Fuller, M.D., Belshé, J.C., Girdler, R.W., 1963. Anisotropy of magnetic susceptibility of rocks and minerals. Journal of Geophysical Research 68, 279–291.

de Wall, H., Bestmann, M., Ullemeyer, K., 2000. Anisotropy of diamagnetic susceptibility in Thassos marble: a comparison between measured and modeled data. Journal of Structural Geology 22, 1761–1771.

Wenk, H.R., 1991. Standard project for pole-figure determination by neutron-diffraction. Journal of Applied Crystallography 24, 920–927.

Wenk, H.R., Takeshita, T., Bechler, E., Erskine, B.G., Matthies, S., 1987. Pure shear and simple shear calcite textures – comparison of experimental, theoretical and natural data. Journal of Structural Geology 9, 731–745.

Woodcock, N.H., 1977. Specification of fabric shapes using an eigenvalue method. Geological Society of America Bulletin 88, 1231–1236.